IOP Publishing Phys. Med. Biol. 65 (2020) 035012 (12pp) https://doi.org/10.1088/1361-6560/ab63ee

Physics in Medicine & Biology

IPEM Institute of Physics and Engineering in Medicine

PAPER

RECEIVED
5 September 2019

REVISED
17 December 2019

ACCEPTED FOR PUBLICATION
19 December 2019

PUBLISHED
4 February 2020

Design study of a brain-dedicated time-of-flight PET system with a hemispherical detector arrangement

Sodai Takyu[1,3], Abdella M Ahmed[1], Eiji Yoshida[1], Hideaki Tashima[1], Masaaki Kumagai[2], Taichi Yamashita[2] and Taiga Yamaya[1]

[1] National Institute of Radiological Sciences, National Institutes for Quantum and Radiological Science and Technology (NIRS-QST), 4-9-1 Anagawa, Inage-ku, Chiba, 263-8555, Japan
[2] ATOX Co. Ltd, 4-11-3 Shiba, Minato-ku, Tokyo 108-0014, Japan
[3] Author to whom any correspondence should be addressed.

E-mail: takyu.soudai@qst.go.jp **and** yamaya.taiga@qst.go.jp

Keywords: positron emission tomography, dedicated brain PET scanner, depth-of-interaction, time-of-flight, coincidence resolving time

Abstract

Time-of-flight (TOF) is now a standard technology for positron emission tomography (PET), but its effective use for small diameter PET systems has not been studied well. In this paper, we simulated a brain-dedicated TOF-PET system with a hemispherical detector arrangement. We modeled a Hamamatsu TOF-PET module (C13500-4075LC-12) with 280 ps coincidence resolving time (CRT), in which a 12 × 12 array of multi pixel photon counters (MPPCs) is connected to a lutetium fine silicate (LFS) crystal array of 4.1 × 4.1 mm^2 cross section each, based on one-to-one coupling. On the other hand, spatial resolution degradation due to the parallax error should be carefully addressed for the small diameter PET systems. The ideal PET detector would have both depth-of-interaction (DOI) and TOF capabilities, but typical DOI detectors that are based on light sharing tend to degrade TOF performance. Therefore, in this work, we investigated non-DOI detectors with an appropriate crystal length, which was a compromise between suppressed parallax error and decreased sensitivity. Using GEANT4, we compared two TOF detectors, a 20 mm long non-DOI and a 10 mm long non-DOI, with a non-TOF, 4-layer DOI detector with a total length of 20 mm (i.e. 5 × 4 mm). We simulated a contrast phantom and evaluated the relationship between the contrast recovery coefficient (CRC) and the noise level (the coefficient of variation, COV) for reconstructed images. The 10 mm long non-DOI, which reduces the parallax error at the cost of sensitivity loss, showed better imaging quality than the 20 mm long non-DOI. For example, the CRC value of a 10 mm hot sphere at COV = 20% was 72% for the 10 mm long non-DOI, which was 1.2 times higher than that of the 20 mm long non-DOI. The converged CRC values for the 10 mm long non-DOI were almost equivalent to those of the non-TOF 4-layer DOI, and the 10 mm long non-DOI converged faster than the non-TOF 4-layer DOI did. Based on the simulation results, we evaluated a one-pair prototype system of the TOF-PET detectors with 10 mm crystal length, which yielded the CRT of 250 ± 8 ps. In summary, we demonstrated support for feasibility of the brain-dedicated TOF-PET system with the hemispherical detector arrangement.

1. Introduction

Positron emission tomography (PET) is a functional imaging modality *in vivo* and widely used for cancer diagnosis. On the other hand, in recent years, aging societies have developed worldwide, and dementia has become a serious social problem. PET is expected to be a powerful tool in the diagnosis of dementia especially for Alzheimer's disease (Klunk *et al* 2004, Okamura *et al* 2009), and a high-performance and affordable brain-dedicated PET scanner is desired.

We previously proposed a compact and high-sensitivity brain-dedicated PET scanner which had a hemispherically arranged detector unit and an add-on detector unit to mitigate the low sensitivity point (Tashima

Table 1. Parameters of the simulated geometries.

	Name (geometry)	Crystal [mm^3]	Array	DOI	TOF	No. of detectors	Geometry
Simulation (this work)	TOF 20 mm	4.1 × 4.1 × 20 mm^3 LFS	12 × 12 × 1	No	280 ps CRT	48	Hemispherical
	TOF 10 mm	4.1 × 4.1 × 10 mm^3 LFS	12 × 12 × 1	No	280 ps CRT		
	Non-TOF DOI	4.1 × 4.1 × 5.0 mm^3 LFS	12 × 12 × 4	4-layer	No		
Prototype (Tashima *et al* 2019)		2.8 × 2.8 × 7.5 mm^3 GSOZ	16 × 16 × 4	4-layer	No	54	Multi-ring

and Yamaya 2016). We developed the first prototype of the system, having the add-on detector at the back of the neck position (the helmet-neck PET), using 4-layered depth-of-interaction (DOI) detectors (Hirano *et al* 2014, Ahmed *et al* 2017a, Tashima *et al* 2019). It was challenging to form a hemisphere by arranging rectangular parallelepiped detectors. In our first prototype, the detector arrangement was based on a multi-ring geometry, in which the radius of each ring was changed so as to form a hemisphere. As an alternative method, we designed a hemispherical detector arrangement, in which the central axis of each detector pointed toward the center of the hemisphere, and a simulation study showed that the hemispherical detector arrangement outperformed the multi-ring detector arrangement in terms of sensitivity (Ahmed *et al* 2017b).

Time-of-flight (TOF) has become a standard technology in PET owing to the recent emergence of photo sensors with excellent timing performance (Schug *et al* 2016, Vandenberghe *et al* 2016, Son *et al* 2017). Whole-body TOF-PET scanners having a time resolution of 400–500 ps have been commercialized (Bettinardi *et al* 2011, Jakoby *et al* 2011, Zaidi *et al* 2011, Burr *et al* 2012, Kolthammer *et al* 2014, Li *et al* 2015, Miller *et al* 2015, Grant *et al* 2016). On the other hand, effective use of TOF for small diameter PET systems has not been studied well. Therefore, in this paper, we investigate feasibility of a brain-dedicated TOF-PET system with the hemispherical detector arrangement.

Using GEANT4, we model PET systems based on a recently released Hamamatsu TOF-PET module (C13500-4075LC-12, Hamamatsu Photonics K.K.) with 280 ps coincidence resolving time (CRT) (Hamamatsu Photonics K.K. 2016). The TOF-PET module has a 12 × 12 array of the multi pixel photon counters (MPPCs) (Kovaltchouk *et al* 2005, Moehrs *et al* 2006, Kim *et al* 2009, Song *et al* 2010, Spanoudaki *et al* 2007), each coupled to a 4.1 × 4.1 × 20 mm^3 lutetium fine silicate (LFS) crystal scintillator (Doroud *et al* 2015) in a one-to-one manner, and electronics circuits to process output of the MPPCs.

On the other hand, spatial resolution degradation due to the parallax error should be carefully addressed for the small diameter PET systems. The ideal PET detector would have both DOI and TOF capabilities, but typical DOI detectors which are based on light sharing tend to degrade TOF performance. Therefore, in this paper, in order to investigate non-DOI detectors with an appropriate crystal length, we compare a TOF-PET detector of 10 mm length with the standard 20 mm length. The shortened length is a compromised solution for the parallax error at the cost of decreased sensitivity. Because TOF information increases the signal-to-noise ratio in PET images according to the equation for the relative sensitivity gain of TOF-PET (Budinger 1983), we expect the good CRT that may be obtained will compensate for the detection efficiency loss in the TOF-PET detector.

2. Material and methods

2.1. Monte Carlo simulation

Table 1 summarizes simulation parameters. Using GEANT4, we modeled three types of detector configurations for the second generation helmet-neck PET prototype based on the first prototype (Tashima *et al* 2019).

The first type configuration had the 20 mm crystal length (TOF 20 mm) which was a standard parameter of the module. The second one had the 10 mm crystal length (TOF 10 mm) because it was expected to cause less parallax error in the peripheral region of the field of view (FOV). The third one was a 5 mm crystal length stacked to have a 4-layer DOI capability but without TOF information (non-TOF DOI). The total crystal length of non-TOF DOI is 20 mm. In the non-TOF DOI, the detector configuration was assumed with 4-layer DOI detection capability based on our light sharing method (Tsuda *et al* 2004). These three geometries had the same number of detectors and LFS scintillators with the same pitch; only crystal length was different. A 280 ps CRT was used for TOF of both 20 mm and 10 mm. The three geometries also had the same hemispherical detector arrangement. The first prototype had the multi-ring detector arrangement which consisted of three detector rings with different radii arranged on the surface of a hemisphere and a top cover detector arranged in a cross-shaped geometry. Figure 1 shows illustrations of detector arrangements of the simulated geometries with the hemispherical detector arrangement.

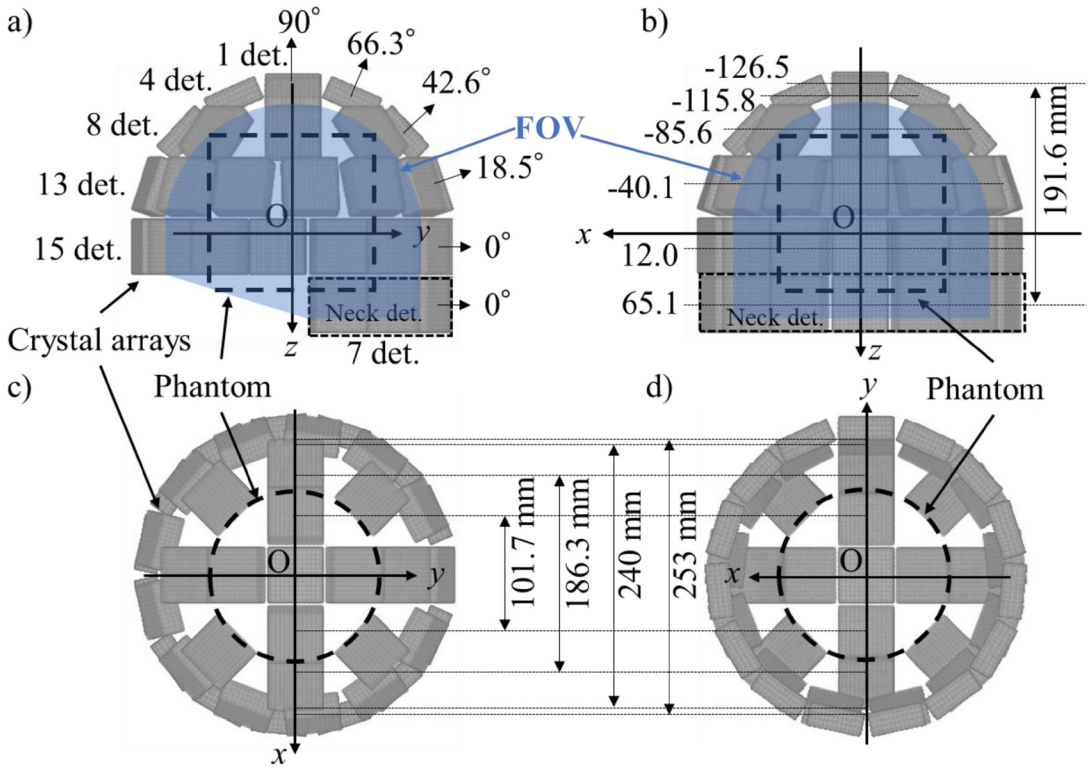

Figure 1. Illustrations of detector arrangement of the simulated geometries with hemispherical detector arrangement. (a) Side view, (b) rear view, (c) top view and (d) bottom view.

The three types of the detector configurations for the second generation prototype had the same ring diameter for each ring as shown in figures 1(c) and (d). In figure 1, gray cuboids are scintillation crystal arrays and regions enclosed by dashed lines indicate the locations of the phantom being simulated. For each ring, the number of arranged detectors and the tilt angle of each detector relative to the *x*-*y* plane are shown in figure 1(a). The locations of the center of the crystal arrays for each ring on the z-axis are also shown in figure 1(b). The FOV was set to the region which was blue colored in figure 1. The center of the FOV was defined as the center of the detector ring with the largest diameter. Contrast phantoms were included inside as shown in figure 2.

The contrast recovery coefficient (CRC) versus noise curve is a widely used metric for quantitative evaluation of the reconstructed images of the whole-body PET scanner with TOF information (Karp *et al* 2008, Surti and Karp 2008, Jakoby *et al* 2011, Thoen *et al* 2013, Surti 2015). These papers reported TOF information improved quality of PET images by increasing the signal-to-noise ratio (SN) from the fact that convergence of the CRC versus noise curve at each region of interest (ROI) in the reconstructed image of the contrast phantom was reached faster with TOF information. Since the evaluation with CRC values is relatively close to clinical conditions, it would be applicable to image quality evaluation of the brain-dedicated PET scanner as well as whole-body PET scanners. Therefore, in this paper, we compared the relationship between CRC and the coefficient of variation (COV) for the ROI set for each radioactive sphere in the reconstructed images of the contrast phantom in the three geometries. The dimensions of the contrast phantom and the ROIs are shown in figures 2(a) and (b). Figure 2(a) is the cross-sectional view from the top and (b) is the side cross-sectional view. The diameters of the hot sphere indicated by the white circle and the ROI number in figures 2(a) and (b) were 10 mm (ROIs 1, 7, 8, 9 and 10), 13 mm (ROI 2), 17 mm (ROI 3), 22 mm (ROI 4), 28 mm (ROI 5) and 37 mm (ROI 6); and the ROI was set with the same size as the hot sphere. This was a phantom modified for the helmet-neck PET with reference to the contrast phantom for the whole-body PET scanner described in NU-2-2012 (National Electrical Manufacturers Association 2012) and IEC Standard 61675-1 (International Electrotechnical Commission 2013). The configuration of the hot spheres which corresponded to ROIs from 1 to 6, was almost the same except for the size. Also, the hot spheres which corresponded to ROIs from 7 to 10 were added to investigate differences of CRC versus COV relationship for hot spheres with the same size at several positions in the FOV because the geometry of the helmet-neck PET is less symmetric compared with conventional cylindrical PET.

The radioactivity ratio of the background region indicated by the gray color and the hot spheres was set to 1:4 ($BG_{true} = 1$, $hot_{true} = 4$). It was assumed that about 20% of the injected 2 mCi (74 MBq) ^{18}F-FDG was accumulated in the brain an hour later. Therefore, the radioactivity in the brain at the start of the measurement was roughly estimated to be 10 MBq. Because this PET scanner was considered to need a shortened scan time as

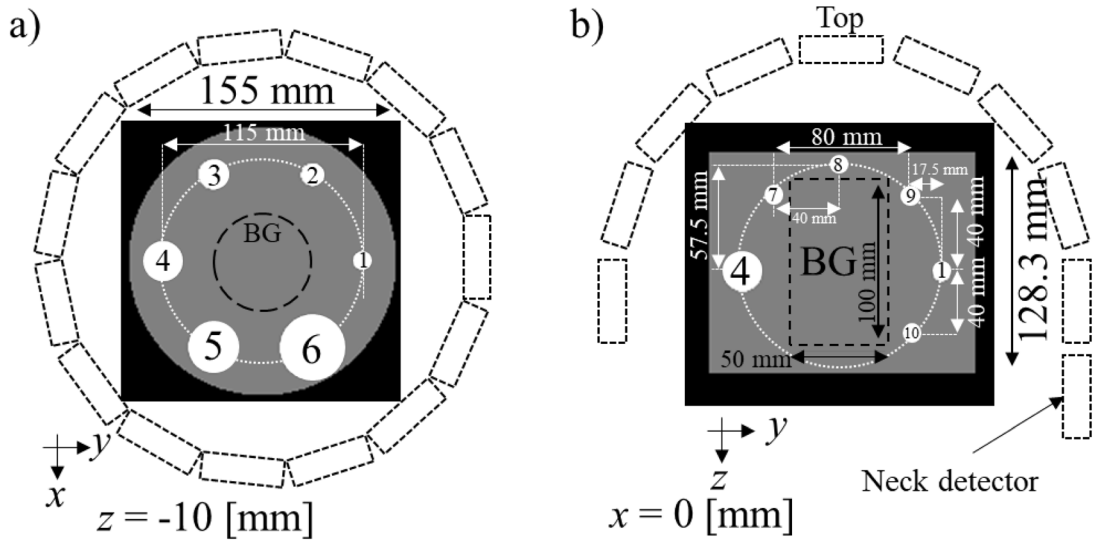

Figure 2. Contrast phantom and its ROI setting: (a) cross-sectional view at $z = -10$ [mm] and (b) side cross-sectional view at $x = 0$ [mm].

a scanner which would be widely used for dementia diagnosis, the scan data in 2 min from the start were analyzed for comparison. Following its estimation, we set the activity which corresponds to approximately 1.2×10^9 beta + decays in the total simulated time. Therefore, 2.4×10^9 annihilation gamma rays were generated in total. Coincidence timing window of the three geometries was assumed to be 10 ns. Each CRC and each COV were calculated by the following equations,

$$\mathrm{CRC}\,[\%] = \frac{\mathrm{hot}_{\mathrm{average}} / \mathrm{BG}_{\mathrm{average}} - 1}{\mathrm{hot}_{\mathrm{true}} / \mathrm{BG}_{\mathrm{true}} - 1} \times 100, \tag{1}$$

$$\mathrm{COV}\,[\%] = \frac{\mathrm{BG}_{\mathrm{SD}}}{\mathrm{BG}_{\mathrm{average}}} \times 100. \tag{2}$$

The areas surrounded by the black dashed lines in figures 2(a) and(b) are the areas defined as BG in equations (1) and (2). The average of the pixel values and the standard deviation in the BG area are $\mathrm{BG}_{\mathrm{average}}$ and $\mathrm{BG}_{\mathrm{SD}}$, respectively. The average of the pixel values in each ROI is $\mathrm{hot}_{\mathrm{average}}$.

For image reconstruction we used TOF list-mode maximum likelihood expectation maximization (ML-EM) (Shepp and Vardi 1982, Parra and Barrett 1998, Groiselle and Glick 2004, Popescu *et al* 2004, Rahmim *et al* 2004, Cui *et al* 2011) for the unique detector arrangement based on our previous development (Tashima *et al* 2019). For the forward and back projection operations, detector response function modeling with a TOF kernel was implemented. The detector response function was modeled using the simple Gaussian function. The size of each image voxel was $1 \times 1 \times 1\,\mathrm{mm}^3$ and the number of the voxels was $280 \times 280 \times 420$. TOF bin size was set to 4 mm, and the TOF kernel was generated by convolving a rectangular function of 4 mm with a Gaussian function representing the TOF resolution (Yamaya *et al* 2000). Normalization was applied using 20 min of measured data of a spherical phantom with the diameter of 248 mm in which total activity of 20 MBq was uniformly distributed and whose center was aligned with the center of the detector ring with the largest diameter in each geometry. In order to purely investigate the effect of noise reduction by using TOF information, the simulation was carried out without attenuation material. Therefore, prompt coincidence was composed of true coincidence and random coincidence in this simulation. The random correction using the single count rates was applied. Scatter and attenuation corrections were not applied.

2.2. Experimental evaluation

Following the simulation, we carried out the single crystal coincidence measurement to investigate the difference of CRT values of 10 mm and 20 mm length LFS using the TOF-PET modules.

Those modules acquired the energy, time, and position information of detected gamma rays in a list-mode data format of single events through the signal processing board (shown in figure 3(b)). The list-mode data of each module were stored in a PC through an external relay board connected to a PCI board. Coincidence detection was carried out by comparing the detection time of the list-mode data offline. These features enabled simultaneous acquisition of the list-mode data by multiple modules. The sub-pixel size of the MPPC was $75 \times 75\,\mu\mathrm{m}^2$.

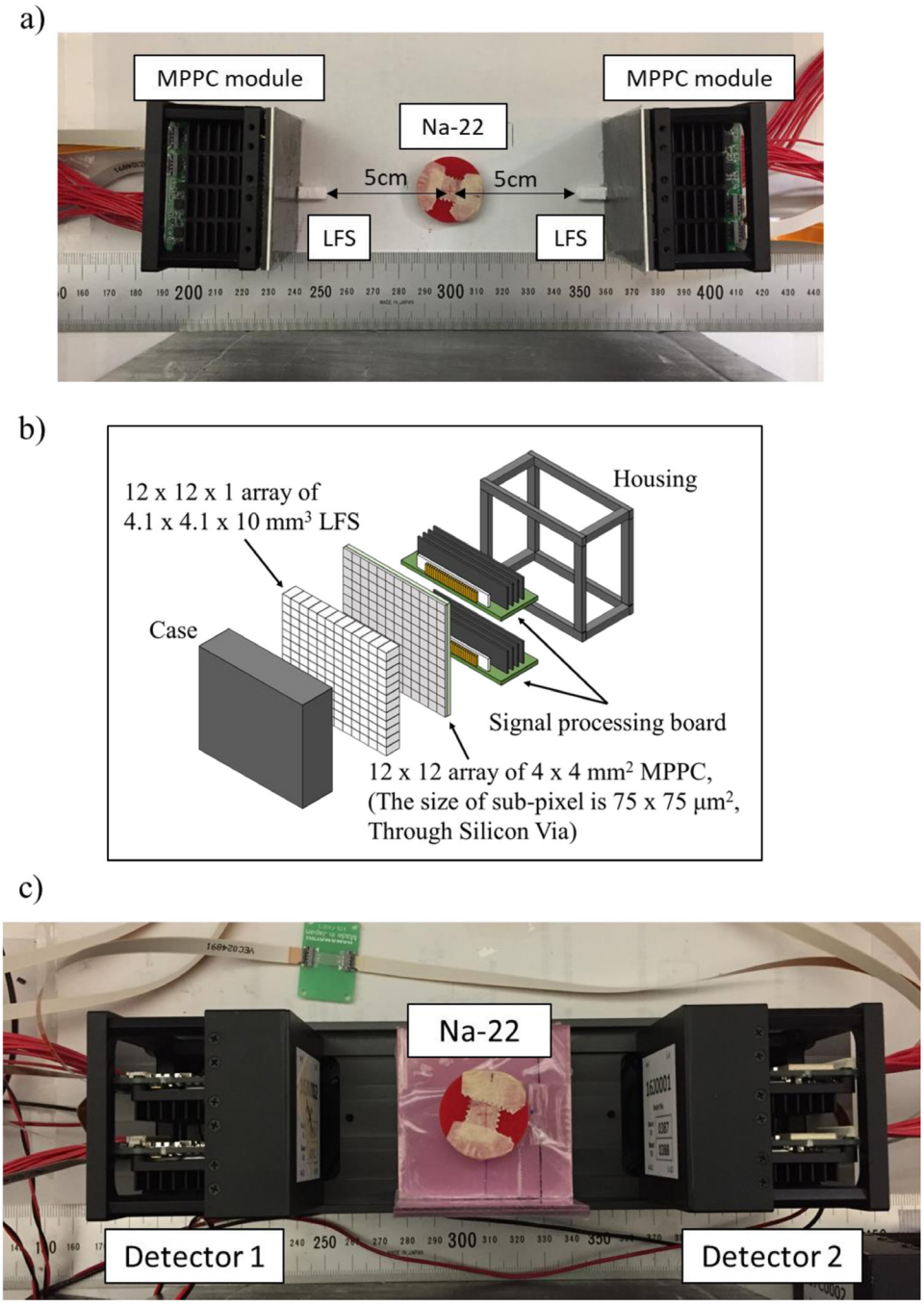

Figure 3. (a) A photo of the single crystal coincidence measurement setup, (b) an illustration of the detector configuration and (c) a photo of the experimental setup for a one-pair prototype.

A pair of 20 mm length LFS crystals ($4.1 \times 4.1 \times 20\,mm^3$) was coupled to one MPPC channel in the two modules, then those modules were placed oppositely. A ^{22}Na point source (1.5 MBq) was placed at the center and the coincidence measurement was performed for 5 min. All crystals were lapped with ESR type films (multilayer polymer mirrors, Sumitomo 3M, Ltd, Japan, 98% reflectivity, 0.065 mm thickness) and Teflon tapes. Optical grease (SC107, Dow Corning Toray Co., Ltd) was used for optical coupling between the crystal and MPPC surface. The coincidence measurement was repeated 5 times. Each crystal was removed and coupled again at each measurement to examine the effect of coupling condition. Also, the same measurements were performed for a pair of 10 mm long LFS crystals. Figure 3(a) is a photo of the single crystal coincidence measurement setup. Coincidence data of the 20–20 mm LFS pair and 10–10 mm LFS pair were obtained. Coincidence timing spectra were obtained by analyzing coincidence data. The energy window was set in the range around 450 to 580 keV. A CRT value was calculated for each timing spectrum.

In addition, we evaluated a one-pair prototype of the TOF-PET detectors based on the TOF-PET module consisting of a 12×12 array of the LFS crystals with the size of $4.1 \times 4.1 \times 10\,mm^3$ and a 12×12 array of the

MPPCs with the size of $4 \times 4\,\mathrm{mm}^2$ as shown in figure 3(b). The center-to-center spacing of the MPPCs was 4.2 mm.

Gamma ray detectors using MPPCs tend to have non-linearity of the output signal for the energy of the gamma rays due to the saturation effect, because a limited number of sub-pixels fire in the case that the number of incident photons becomes larger than the number of sub-pixels which are able to respond (Otte *et al* 2005, Nassalski *et al* 2010, Gruber *et al* 2014). The effect becomes serious as the gamma ray energy increases. To investigate the effect and convert the output signal to accurate energy information, a relationship between gamma ray energy and pulse height (analog-to-digital-converter (ADC) channel) was investigated using point sources with different energies (^{22}Na (511 and 1275 keV peaks were used), ^{137}Cs (662 keV), ^{152}Eu (122, 245, 344, 779 and 1408 keV), ^{176}Lu (202 and 307 keV), ^{54}Mn (834 keV) and ^{133}Ba (80 and 356 keV)). The relationship can be modeled by a saturation curve as follows:

$$y = a \times \left(1 - \exp\left(\frac{-\varepsilon x}{a}\right)\right), \tag{3}$$

and the energy calibration was carried out (Otte *et al* 2005, Nassalski *et al* 2010, Gruber *et al* 2014). For equation (3), y is the ADC channel, x is energy [keV], a is the effective pixel number of an MPPC, and ε is a constant. The a and ε values were calculated by the fitting, and the ADC channel of the acquired list-mode data was converted to energy [keV] by using the inverse function of equation (3). After energy correction, the averaged energy resolution at 511 keV in 144 channels was calculated in two detectors.

Next, those two detectors were oppositely placed with a 12 cm distance between them. A ^{22}Na point source (1.5 MBq) was placed at the center and the coincidence measurement was performed for 10 min (figure 3(c)). After coincidence processing, timing spectrum for each channel was obtained. The energy window of 450–580 keV was applied. Due to the characteristics of circuits such as the field-programmable gate array (FPGA) in the front-end electronics of this module, there can be variation of the time stamp between each channel (van Dam *et al* 2013). Variation of the time stamp deteriorates the estimation accuracy of detection time for coincidence. However, that variation can be corrected if it can be figured out beforehand. Therefore, the time stamp for each channel was investigated from those timing spectra for timing correction. Approximately 10 000–15 000 coincidence events for each channel were used to measure the time stamp. The overall timing spectrum with and without timing correction was obtained by adding those timing spectra.

3. Results

3.1. Monte Carlo simulation

In 1.2×10^9 decays of the 2 min simulation, the number of prompt coincidence events was 145 M counts in non-TOF DOI, 145 M counts in TOF 20 mm and 67.2 M counts in TOF 10 mm. The number of true coincidence events was 118 M counts in non-TOF DOI, 118 M counts in TOF 20 mm and 52.5 M counts in TOF 10 mm. TOF 10 mm showed lowest true coincidence counts. Random fraction was 18.6% in non-TOF DOI, 18.6% in TOF 20 mm and 21.9% in TOF 10 mm. TOF 20 mm and non-TOF DOI showed the same count rate characteristics because of the same crystal length in total and the same coincidence timing window. The number of true coincidence events was reduced by a factor of 0.44 when changing the LFS length from 20 mm to 10 mm.

Figure 4 shows reconstructed images of the contrast phantom for each iteration number and each geometry. Figure 4(a) is a top view and (b) is a cross-sectional view. The images with TOF information were sharper than without TOF information at low iteration numbers. Although most of the 10 mm spheres looked burred in all images at five iterations, almost all of them could be clearly observed with increasing iteration number. On the other hand, the variation of noise (especially in the background region) looked to be increasing with increasing iteration number. The images which have outer frames with the same color (red, green and blue) show almost the same COV values in figure 4. Comparing those images, there was no significant difference in TOF 10 mm images for the other two geometries, despite the geometry with TOF 10 mm having the smallest number of events.

Figure 5 shows graphs of the relationship between CRC and COV for each ROI (each hot sphere). Each CRC versus COV relationship was plotted for every five iterations for a total of 100 iterations. The image of the left-most bottom and that of the top right correspond to images at the iteration numbers of 5 and 100 in each CRC versus COV relationship, respectively.

The smaller the diameter of the hot sphere was, the more iterations were required to converge the CRC value. When the CRC value of the 10 mm diameter hot sphere reached approximately its maximum, the numbers of iterations of TOF 10 mm, TOF 20 mm and non-TOF DOI were 20, 50 and 100, respectively. The difference of the CRC values was small for the larger hot spheres. Since the influence of parallax error became stronger in the smaller hot spheres, the converged CRC values of TOF 20 mm decreased. For the 10 mm diameter hot spheres, the converged CRC values of TOF 20 mm were about 20% lower than those of TOF 10 mm. Although the converged

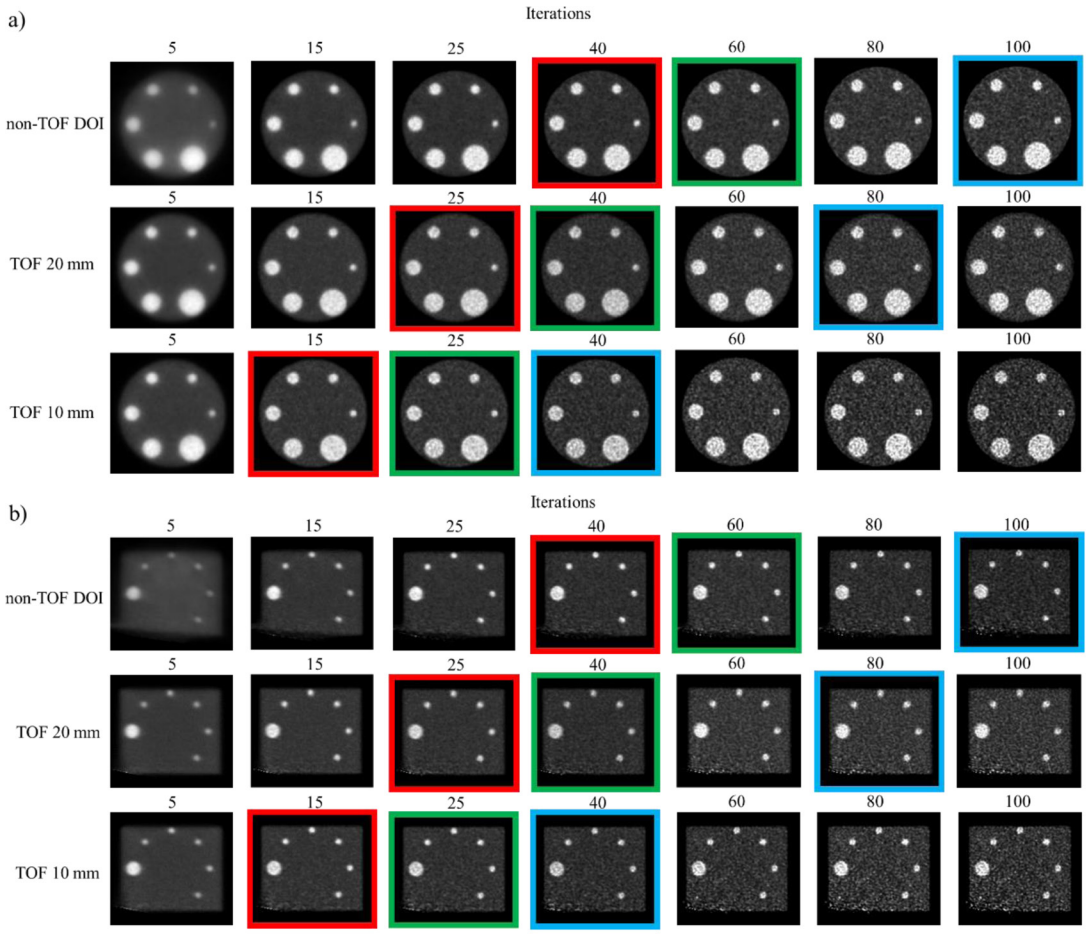

Figure 4. Reconstruction images of contrast phantom with each geometry and iteration, (a) top view and (b) side cross-sectional view. The images which have outer frames with the same color (red, green and blue) show almost the same COV values.

CRC values of TOF 10 mm were similar to those of non-TOF DOI in all hot spheres, TOF 10 mm converged with lower iteration number than non-TOF DOI did.

3.2. Experimental evaluation

Figure 6 is the normalized coincidence timing spectrum at one of the five single crystal coincidence measurements. The horizontal axis of this graph shows the time difference [ps] between detector pairs which had coincidence detection. The time between adjacent points in figure 6 is 15.625 ps which means the bin size of the time-to-digital-converter (TDC). Because maximum counts in the timing spectrum of the 20–20 mm LFS pair were 2.5 times larger than the 10–10 mm LFS pair, each timing spectrum was normalized by the respective maximum count. In figure 6, CRT values of the 20–20 mm LFS pair and 10–10 mm LFS pair were 285 ps FWHM and 253 ps FWHM, respectively. The averaged CRT values in five coincidence measurements were 286.2 $\pm$ 4.1 ps FWHM in 20–20 mm LFS pair and 253.6 $\pm$ 2.4 ps FWHM in 10–10 mm LFS pair. We repeated the same measurements in other MPPC channels and confirmed the variation of CRT values was not significant. Therefore, the differences of CRT values of 10 mm and 20 mm length LFS in the single crystal coincidence measurement were expected to be around 30 ps FWHM.

Figure 7(a) shows the relationship between gamma ray energy and the ADC channel on one of the prototyped detectors. Linearity degradation due to the MPPC saturation was seen. Compared to the yellow straight line of figure 7(a) which was drawn by assuming no linearity degradation, the linearity degradation was about 37% at 511 keV.

Figure 7(b) shows the ^{22}Na energy spectrum after the energy correction at one of the channels of detector 1. The averaged energy resolution at 511 keV after the energy correction was 11.7% $\pm$ 0.7% for detector 1 and 11.6% $\pm$ 0.8% for detector 2. Since the energy resolution of commercial PET scanners in recent years has been in the range of 10%–15%, those values were reasonable.

The averaged CRT value in 144 channels was 250 $\pm$ 8 ps FWHM. Because variation of the time stamp was observed in the timing spectrum for each channel as expected, we performed the timing correction for each pair of crystals. Figure 8 is the overall timing spectrum with and without timing correction on a one-pair prototype.

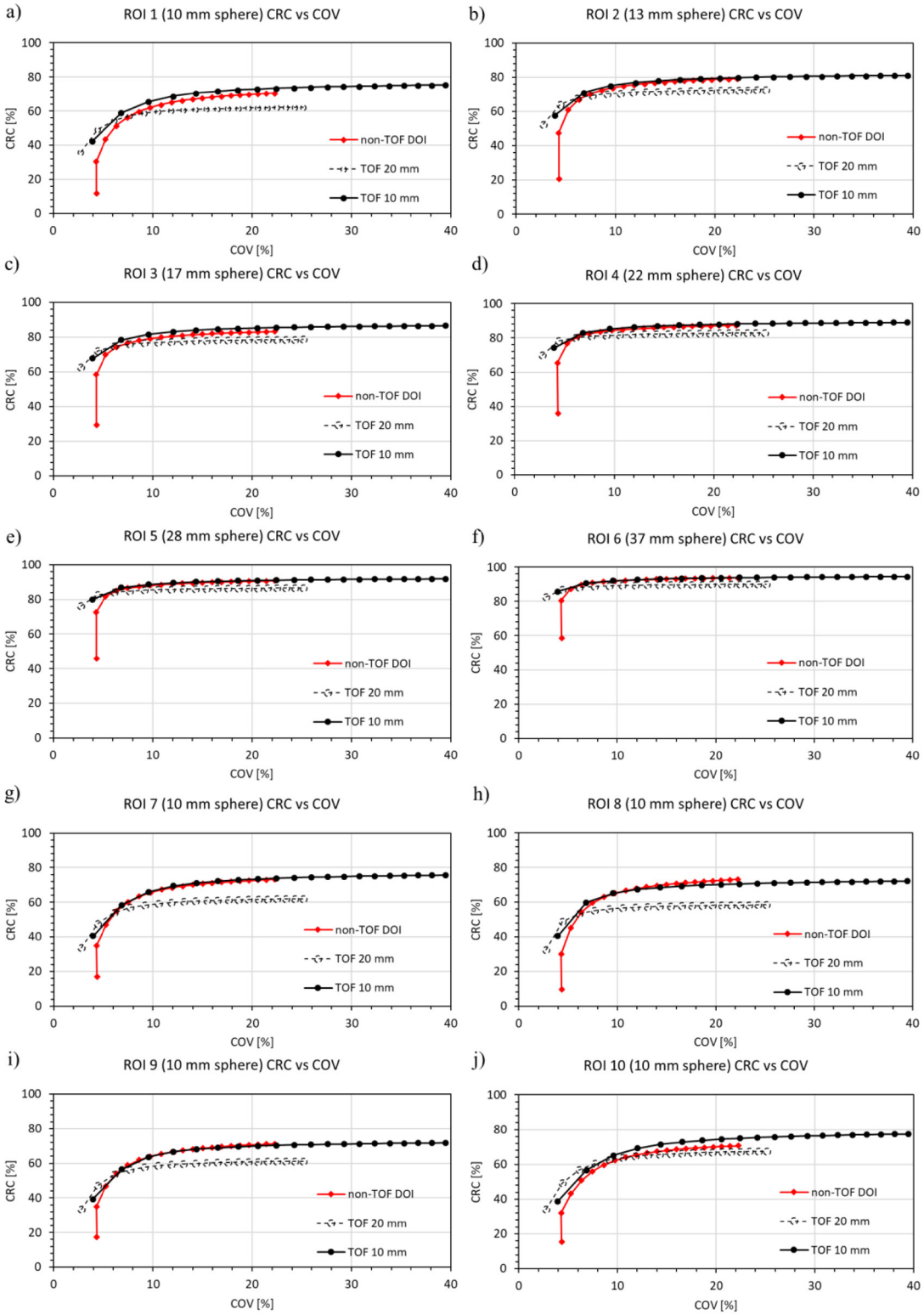

Figure 5. CRC versus COV relationship in three geometries for each ROI: (a) ROI 1 (10 mm sphere), (b) ROI 2 (13 mm sphere), (c) ROI 3 (17 mm sphere), (d) ROI 4 (22 mm sphere), (e) ROI 5 (28 mm sphere), (f) ROI 6 (37 mm sphere), (g) ROI 7 (10 mm sphere), (h) ROI 8 (10 mm sphere), (i) ROI 9 (10 mm sphere) and (j) ROI 10 (10 mm sphere). Each CRC versus COV relationship was plotted for every five iterations for a total of 100 iterations.

The horizontal axis shows detection time difference [ps]. The time between adjacent points was 15.625 ps as mentioned in figure 6. The CRT value as an overall detector without timing correction was 480 ps FWHM. On the other hand, the CRT value as an overall detector with timing correction was 250 ps FWHM.

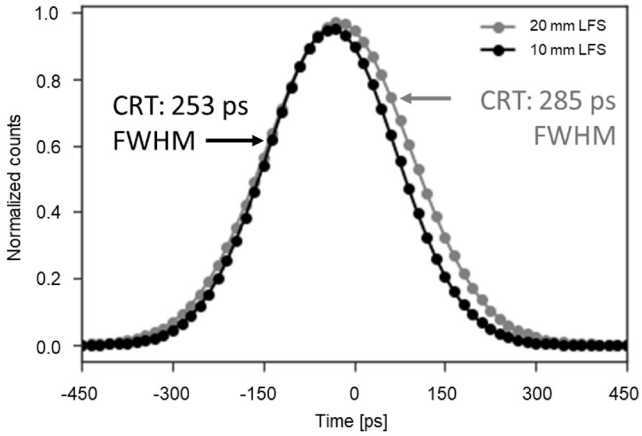

Figure 6. Normalized coincidence timing spectra at the single crystal coincidence measurement.

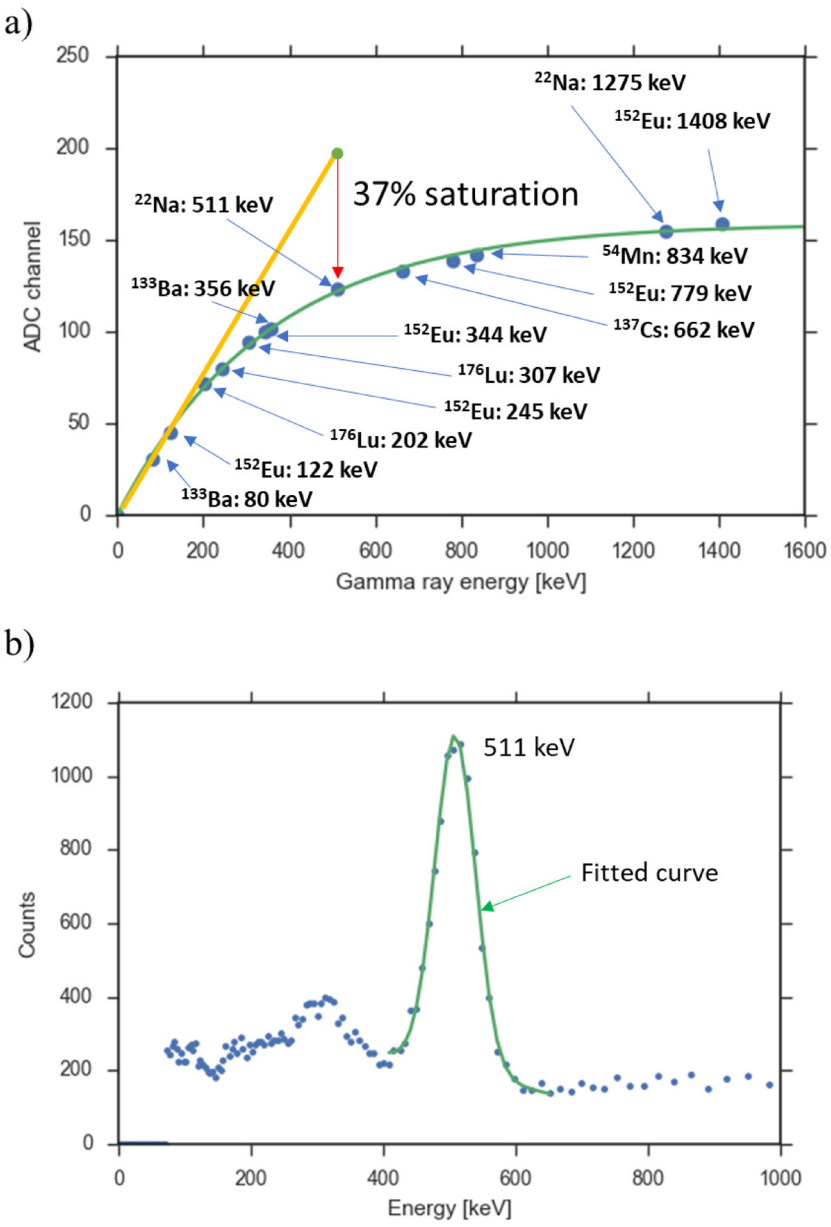

Figure 7. Energy correction: (a) a relationship between the gamma ray energy and ADC channel and (b) a Na-22 spectrum after saturation correction.

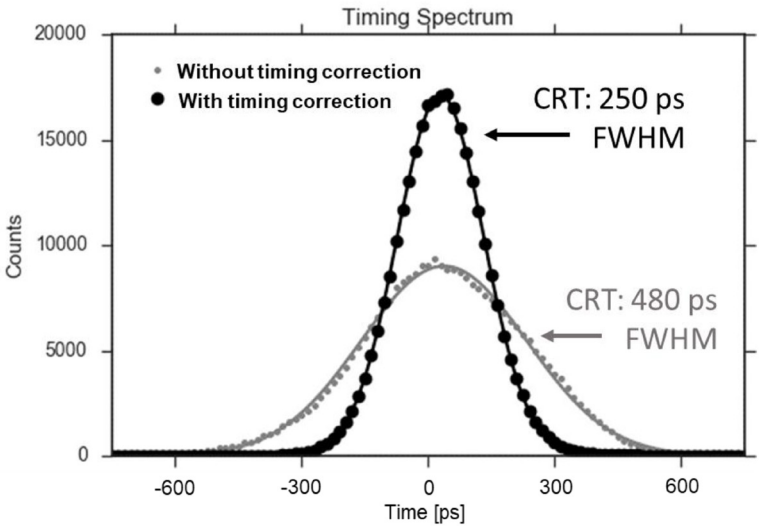

Figure 8. Overall timing spectra with and without timing correction.

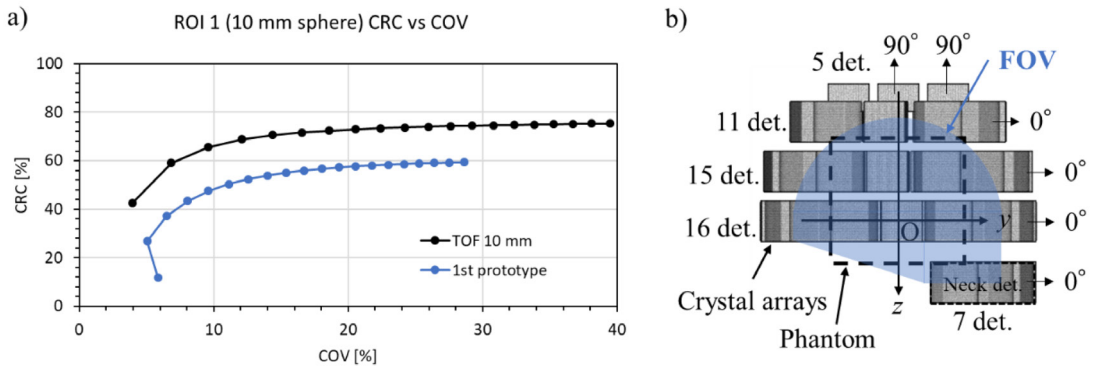

Figure 9. (a) A comparison of CRC versus COV relationship between TOF 10 mm and first prototype at ROI 1 (10 mm sphere). (b) An illustration of the simulated geometry of the first prototype with multi-ring detector arrangement.

4. Discussion

We investigated feasibility of TOF information use for the brain-dedicated TOF-PET system with the hemispherical detector arrangement.

In the simulation, the coincidence timing window of non-TOF DOI, TOF 20 mm and TOF 10 mm was virtually set to 10 ns based on commercial TOF-PET scanners (Vandenberghe *et al* 2016). Because the TOF-PET scanners have around a 4–5 ns coincidence timing window, TOF 20 mm and TOF 10 mm with the CRT value of 280 ps would be able to be set to a narrower coincidence timing window in actual use. Therefore, the results of the CRC versus COV relationship would be changed slightly in reality.

From the results of the CRC versus COV relationship, it was expected that TOF 10 mm would be the best among the three geometries from the viewpoint of the convergence speed and the contrast recovery for all hot spheres. The crystal pitch of 4.1 mm may seem large for a brain dedicated system compared with previous studies (Kolb *et al* 2012, Hong *et al* 2013, Bauer *et al* 2016); however, the one-to-one crystal-SiPM coupling can minimize the cross talk between crystal segments which is often seen in typical PET detectors based on the light sharing method. Therefore, actual crystal identification performance would be comparative to that of light sharing PET detectors with smaller crystal pitch. Also, an additional advantage for TOF 10 mm over the non-TOF DOI would be lower manufacturing cost because the 4-layer detector needs many crystal blocks made.

With reference to the relationship between TOF, crystal size and DOI, Theon *et al* (2013) reported that the introduction of two-layer DOI information only led to a modest improvement in whole-body PET scanner performance, unlike TOF and crystal size. In this study, we investigated the CRC versus COV relationship for the brain-dedicated PET scanner which had a smaller ring diameter and approximately two times improved TOF resolution compared with typical whole-body PET scanners. TOF 20 mm and non-TOF DOI each had the same detector arrangement, crystal cross section and crystal length, and they differed only for DOI or TOF. Also,

the numbers of obtained events were the same. The results showed non-TOF DOI was better in image quality than TOF 20 mm with 280 ps CRT. We found that the DOI information would be relatively more effective than TOF information in the PET scanner with a small ring diameter under the conditions of the same total crystal length. However, in this study, TOF 10 mm having small parallax error without DOI information showed the best performance for the second generation prototype of the helmet-neck PET while the numbers of detected true coincidence events were small. We speculated that the TOF gain and reduced parallax error of TOF 10 mm compensated for the decreased sensitivity due to shortened crystal length in the brain-dedicated PET system. Therefore, we decided to adopt TOF 10 mm.

As a reference, the CRC versus COV relationship of TOF 10 mm was compared with that of the first prototype (Tashima *et al* 2019) using the same contrast phantom in this study. TOF 10 mm showed better CRC versus COV relationship than the first prototype for all hot spheres. Figure 9(a) summarizes the results at ROI 1 as an example and (b) is the detector arrangement of the first prototype.

In the experimental evaluation, the CRT value obtained with the crystal size of $4.1 \times 4.1 \times 10\,\mathrm{mm}^3$ was 250 ps, and it was 30 ps better than the CRT value of 280 ps obtained with the crystal size of $4.1 \times 4.1 \times 20\,\mathrm{mm}^3$. The reason for the difference of the CRT values in the crystal lengths of 10 mm and 20 mm was presumed to be that the average optical path length of photons reaching the MPPC surface became shorter as the crystal length became shorter.

Considering the literature (Budinger 1983, Conti 2009) which describes the TOF gain, we can expect a brain-dedicated TOF-PET system with the timing resolution of 250 ps CRT to have a potential TOF gain comparable to that of recent commercialized whole-body TOF-PET scanners with a time resolution of around 500 ps CRT.

5. Conclusion

We investigated the feasibility of the brain-dedicated TOF-PET system with the hemispherical detector arrangement. The CRC versus COV relationship was investigated to compare imaging performance for three detector configurations by the simulation study using the contrast phantom. The results suggested that TOF 10 mm would be the best among the three geometry configurations, despite it having the smallest number of events.

In summary, we obtained the results from simulation and experiment which had high usefulness and supported the feasibility of the second generation prototype of the helmet-neck PET using the TOF-PET detector with 250 ps CRT timing resolution. We expect that the system will become a key factor in successfully accelerating the dissemination of high performance and cost-effective brain-dedicated PET scanners for early diagnosis of dementia.

Acknowledgments

This work was partially supported by the Japan Society for the Promotion of Science (JSPS) KAKENHI Grant Nos. 17K18378 and 16K21637.

References

Ahmed A, Tashima H, Yoshida E and Yamaya T 2017b Investigation of the optimal detector arrangement for the helmet-chin PET—a simulation study *Nucl. Instrum. Methods Phys. Res.* A **858** 96–100

Ahmed A, Tashima H, Yoshida E, Nishikido F and Yamaya T 2017a Simulation study comparing the helmet-chin PET with a cylindrical PET of the same number of detectors *Phys. Med. Biol.* **62** 4541–50

Bauer C E *et al* 2016 Concept of an upright wearable positron emission tomography imager in humans *Brain Behav.* **6** 1–10

Bettinardi V, Presotto L, Rapisarda E, Picchio M, Gianolli L and Gilardi M C 2011 Physical performance of the new hybrid PET/CT Discovery-690 *Med. Phys.* **38** 5394–411

Budinger T F 1983 Time-of-flight positron emission tomography: status relative to conventional PET *J. Nucl. Med.* **24** 73–8

Burr K C *et al* 2012 A new modular and scalable detector for a time-of-flight PET scanner *Nuclear Science Symp. and Medical Imaging Conf.* (IEEE) pp 2830–4

Conti M 2009 State of the art and challenges of time-of-flight PET *Phys. Med.* **25** 1–11

Cui J-Y, Pratx G, Prevrhal S and Levin C S 2011 Fully 3D list-mode time-of-flight PET image reconstruction on GPUs using CUDA *Med. Phys.* **38** 6775–86

Doroud K, Williams M C S, Zichichi A and Zuyeuski R 2015 Comparative timing measurements of LYSO and LFS-3 to achieve the best time resolution for TOF-PET *Nucl. Instrum. Methods Phys. Res.* A **793** 57–61

Grant A M, Deller T W, Khalighi M M, Maramraju S H, Delso G and Levin C S 2016 NEMA NU 2-2012 performance studies for the SiPM-based ToF-PET component of the GE SIGNA PET/MR system *Med. Phys.* **43** 2334–43

Groiselle C J and Glick S J 2004 3D PET list-mode iterative reconstruction using time-of-flight information *Conf. Record of the 2004 IEEE Nuclear Science Symp. and Medical Imaging Conf. (Rome, Italy, 20–22 October 2004)* pp M02–305

Gruber L, Brunner S E, Marton J and Suzuki K 2014 Over saturation behavior of SiPMs at high photon exposure *Nucl. Instrum. Methods Phys. Res.* A **737** 11–8

Hamamatsu Photonics K.K. 2016 MPPC module for PET (www.hamamatsu.com/resources/pdf/ssd/pet_module_kacc0011e.pdf)

Hirano Y, Nitta M, Inadama N, Nishikido F, Yoshida E, Murayama H and Yamaya T 2014 Performance evaluation of a depth-of-interaction detector by use of position-sensitive PMT with a super-bialkali photocathode *Radiol. Phys. Technol.* **7** 57–66
Hong K J *et al* 2013 A prototype MR insertable brain PET using tileable GAPD arrays *Med. Phys.* **40** 1–12
International Electrotechnical Commission (IEC) 2013 Radionuclide imaging devices—characteristics and test conditions. Part 1. Positron emission tomographs *Standard Report 61675-1:2013* IEC
Jakoby B W, Bercier Y, Conti M, Casey M E, Bendriem B and Townsend D W 2011 Physical and clinical performance of the mCT time-of-flight PET/CT scanner *Phys. Med. Biol.* **56** 2375–89
Karp J S, Surti S, Daube-Witherspoon M E and Muehllehner G 2008 Benefit of time-of-flight in PET: experimental and clinical results *J. Nucl. Med.* **49** 462–70
Kim C L, Wang G-C and Dolinsky S 2009 Multi-pixel photon counters for TOF PET detector and its challenges *IEEE Trans. Nucl. Sci.* **56** 2580–5
Klunk W *et al* 2004 Imaging brain amyloid in Alzheimer's disease with Pittsburgh Compound-B *Ann. Neurol.* **55** 306–19
Kolb A *et al* 2012 Technical performance evaluation of a human brain PET/MRI system *Eur. Radiol.* **22** 1776–88
Kolthammer J A, Su K H, Grover A, Narayanan M, Jordan D W and Muzic R F 2014 Performance evaluation of the Ingenuity TF PET/CT scanner with a focus on high count-rate conditions *Phys. Med. Biol.* **59** 3843–59
Kovaltchouk V D, Lolos G J, Papandreou Z and Wolbaum K 2005 Comparison of a silicon photomultiplier to a traditional vacuum photomultiplier *Nucl. Instrum. Methods Phys. Res.* A **538** 408–15
Li H, Ruixue C, Haiqun X, Nan L, Cheng Z, Heyu W, Yuan-chuan T, Fang L and Hui Z 2015 Performance evaluation of a new high-sensitivity TOF clinical PET/CT system, *J. Nucl. Med.* **56** 433
Miller M, Zhang J, Binzel K, Griesmer J, Laurence T, Narayanan M, Natarajamani D, Wang S and Knopp M 2015 Characterization of the vereos digital photon counting PET system *J. Nucl. Med.* **56** 434
Moehrs S, Del Guerra A, Herbert D J and Mandelkern M A 2006 A detector head design for small-animal PET with silicon photomultipliers (SiPM) *Phys. Med. Biol.* **51** 1113–27
Nassalski A, Moszynski M, Syntfeld-Kazuch A, Szczesniak T, Swiderski L, Wolski D, Batsch T and Baszak J 2010 Multi pixel photon counters (MPPC) as an alternative to APD in PET applications *IEEE Trans. Nucl. Sci.* **57** 1008–14
National Electrical Manufacturers Association (NEMA) 2012 *NU-2-2012: Performance Measurements of Positron Emission Tomographs* (Rosslyn, VA: NEMA)
Okamura N, Fodero-Tavoletti M, Kudo Y, Rowe C, Furumoto S, Arai H, Masters C, Yanai K and Villemagne V 2009 Advances in molecular imaging for the diagnosis of dementia *Expert Opin. Med. Diagn.* **3** 705–16
Otte A N, Barral J, Dolgoshein B, Hose J, Klemin S, Lorenz E, Mirzoyan R, Popova E and Teshima M 2005 A test of silicon photomultipliers as readout for PET *Nucl. Instrum. Methods Phys. Res.* A **545** 705–15
Parra L C and Barrett H H 1998 List-mode likelihood: EM algorithm and image quality estimation demonstrated on 2D-PET *IEEE Trans. Med. Imaging* **17** 228–35
Popescu L M, Matej S and Lewitt R M 2004 Iterative image reconstruction using geometrically ordered subsets with list-mode data *Conf. Record of the 2004 IEEE Nuclear Science Symp. and Medical Imaging Conf. (Rome, Italy, 20–22 October 2004)* pp M09–211
Rahmim A, Lenox M, Reader A J, Michel C, Burbar Z, Ruth T J and Sossi V 2004 Statistical list-mode image reconstruction for the high resolution research tomograph *Phys. Med. Biol.* **49** 4239–58
Schug D *et al* 2016 Initial PET performance evaluation of a preclinical insert for PET/MRI with digital SiPM technology *Phys. Med. Biol.* **61** 2851–78
Shepp L and Vardi Y 1982 Maximum likelihood reconstruction for emission tomography *IEEE Trans. Med. Imaging* **1** 113–22
Son J W, Kim K Y, Yoon H S, Won J Y, Ko G B, Lee M S and Lee J S 2017 Proof-of-concept prototype time-of-flight PET system based on high-quantum-efficiency multianode PMTs *Med. Phys.* **44** 5314–24
Song T Y, Wu H, Komarov S, Siegel S B and Tai Y-C 2010 A sub-millimeter resolution PET detector module using a multi-pixel photon counter array *Phys. Med. Biol.* **55** 2573–87
Spanoudaki V C, Mann A B, Otte A N, Konorov I, Torres-Espallardo I, Paul S and Ziegler S I 2007 Use of single photon counting detector arrays in combined PET/MR: characterization of LYSO-SiPM detector modules and comparison with a LSO-APD detector *J. Instrum.* **2** P12002
Surti S 2015 Update on time-of-flight PET imaging *J. Nucl. Med.* **56** 98–105
Surti S and Karp J S 2008 Design considerations for a limited angle, dedicated breast, TOF PET scanner *Phys. Med. Biol.* **53** 2911–21
Tashima H and Yamaya T 2016 Proposed helmet PET geometries with add-on detectors for high sensitivity brain imaging *Phys. Med. Biol.* **61** 7205–20
Tashima H *et al* 2019 First prototyping of a dedicated PET system with the hemisphere detector arrangement *Phys. Med. Biol.* **64** 065004
Thoen H, Keereman V, Mollet P, Van Holen R and Vandenberghe S 2013 Influence of detector pixel size, TOF resolution and DOI on image quality in MR-compatible whole-body PET *Phys. Med. Biol.* **58** 6459–79
Tsuda T, Murayama H, Kitamura K, Yamaya T, Yoshida E, Omura T, Kawai H, Inadama N and Orita N 2004 A four-layer depth-of-interaction detector block for small animal PET *IEEE Trans. Nucl. Sci.* **51** 2537–42
van Dam H T, Borghi G, Seifert S and Schaart D R 2013 Sub-200 ps CRT in monolithic scintillator PET detectors using digital SiPM arrays and maximum likelihood interaction time estimation *Phys. Med. Biol.* **58** 3243–57
Vandenberghe S, Mikhaylova E, D'Hoe E, Mollet P and Karp J S 2016 Recent developments in time-of-flight PET *EJNMMI Phys.* **3** 1–30
Yamaya T, Obi T, Yamaguchi M and Ohyama N 2000 High-resolution image reconstruction method for time-of-flight positron emission tomography *Phys. Med. Biol.* **45** 3125–34
Zaidi H *et al* 2011 Design and performance evaluation of a whole-body Ingenuity TF PET-MRI system *Phys. Med. Biol.* **56** 3091–106